

Instantaneous velocity during quantum tunnelling

Xiao-Wen Shang,^{1,2,*} Jian-Peng Dou,^{1,2,†} Feng Lu,^{1,2} Sen Lin,³ Hao Tang,^{1,2,‡} and Xian-Min Jin^{1,2,4,5,§}

¹*Center for Integrated Quantum Information Technologies (IQIT),
School of Physics and Astronomy and State Key Laboratory of Photonics and Communications,
Shanghai Jiao Tong University, Shanghai 200240, China*

²*Hefei National Laboratory, Hefei 230088, China*

³*School of mathematics and statistics, Jiangsu Normal University, Xuzhou 221009, China*

⁴*Chip Hub for Integrated Photonics Xplore (CHIPX),
Shanghai Jiao Tong University, Wuxi 214000, China*

⁵*TuringQ Co., Ltd., Shanghai 200240, China*

Quantum tunnelling, a hallmark phenomenon of quantum mechanics, allows particles to pass through the classically forbidden region. It underpins fundamental processes ranging from nuclear fusion and photosynthesis to the operation of superconducting qubits. Yet the underlying dynamics of particle motion during tunnelling remain subtle and are still the subject of active debate. Here, by analyzing the temporal evolution of the tunnelling process, **we show that the particle velocity inside the barrier continuously relaxes from a large initial value toward a smaller one, and may even approach zero in the evanescent regime. Meanwhile, the probability density within the barrier gradually builds up before reaching its stationary profile, in contrast to existing inherently.** In addition, starting from the steady-state equations, we derive an explicit relation between the particle velocity and the barrier width, and show that the velocity in evanescent states approaches zero when the barrier is sufficiently wide. These findings resolve the apparent paradox of a vanishing steady-state velocity coexisting with a finite particle density. We point out that defining an effective speed from the probability density, rather than from the probability current, can lead to spuriously nonzero “stationary speed,” as appears to be the case in Ref. [Nature 643, 67 (2025)]. Our work establishes a clear dynamical picture for the formation of tunnelling flow and provides a theoretical foundation for testing time-resolved tunnelling phenomena.

INTRODUCTION

In the classical world, when the water level rises above a river weir, a small boat can be carried smoothly across by the flowing water, as shown in Fig. 1(a). By contrast, when the water level is well below the height of the weir, the boat—being a classical macroscopic object—is blocked and cannot pass. Quantum tunnelling, however, allows particles to traverse classically forbidden potential barriers even when their kinetic energy is insufficient to surmount them. An intuitive analogy would be a boat crossing the weir even at low water levels, as illustrated in Fig. 1(b). Meanwhile, the particle has a nonzero probability of residing inside the barrier, as well as a nonzero probability of being reflected, as illustrated by the boat-weir analogy in Fig. 1(c). Yet the microscopic dynamics of tunnelling—particularly what occurs inside the barrier—remain under active theoretical debate [1–4] and increasingly precise experimental scrutiny [5–11].

When the incident particle energy E lies below the barrier height V , the wave vector inside the barrier becomes imaginary, leading to an evanescent state. For a sufficiently wide barrier, the wave function decays exponentially as $e^{-\kappa x}$, where $\kappa = \sqrt{2m(V-E)}/\hbar$ is the decay constant. The question of tunnelling time in this regime has long been controversial and continues to stimulate significant theoretical and experimental advances. A central challenge is that, although the Schrödinger equation governs the full evolution of the quantum state,

it does not explicitly provide a local velocity from its standard formulation. Beyond the direct solution of the Schrödinger equation, one may rewrite the wave function in polar form, $\psi(x,t) = \sqrt{\rho(x,t)}e^{iS(x,t)}$, and substitute it into the Schrödinger equation to obtain the gradient of the phase S , which defines a velocity field,

$$\mathbf{v}(x,t) = \frac{\hbar}{m} \nabla S(x,t). \quad (1)$$

This velocity, introduced by Bohm in 1952, is known as the Bohmian velocity [12]. It follows directly from the wave function and the Schrödinger equation and is fully consistent with the continuity equation [13, 14]. From a mathematical standpoint, it is therefore well-defined within quantum mechanics.

Nevertheless, the physical interpretation and empirical relevance of this velocity have been the subject of renewed debate in recent [15–22]. This discussion was stimulated by an elegant optical experiment reported by Sharoglazova et al. [23, 24], in which population transfer between two coupled photonic waveguides was used as a clock. In this approach, the speed is inferred from the relative probability densities in the two waveguides. This method is commonly used to estimate the propagation speed of guided propagating modes, rather than evanescent modes, in coupled waveguide systems. On the other hand, using an interference-based approach, they observed that the Bohmian speed within evanescent states approaches zero. This zero Bohmian velocity differs from the velocity inferred from the relative prob-

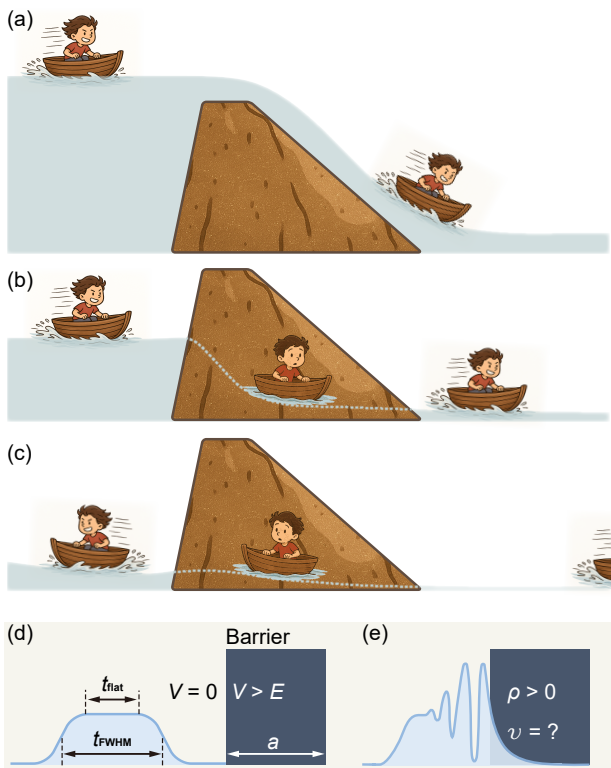


FIG. 1. Schematic illustration of the particle dynamics upon encountering a potential barrier. (a) When a particle’s energy exceeds the barrier height, the particle easily traverses the barrier, analogous to a boat moving over a weir when the water level is higher than the barrier. (b) When a particle’s energy lies below the barrier height, quantum tunnelling permits it to enter the classically forbidden region, where its velocity may slow to nearly zero. This behavior is analogous to a boat whose water level lies below a weir: although classical intuition would forbid passage, the boat can nonetheless cross with a finite probability and momentarily come to rest within the barrier. (c) Once the wave is reflected, the nearly stationary “boat” inside the barrier is driven backward, propagating out of the barrier and regaining its pre-barrier speed. (d) The incident wave packet is modeled as a pulse with Gaussian rising and falling edges, featuring a full width at half maximum of $t_{\text{FWHM}} = 1.14$ ns and a flat-top duration of $t_{\text{flat}} = 0.86$ ns. The barrier width is denoted by a . In the limit $a \rightarrow \infty$, the barrier becomes semi-infinite. (e) A schematic of the probability density distribution ρ of a particle encountering the barrier. This work presents the time evolution of the particle velocity v inside the barrier and elucidates its dependence on the barrier width a .

ability densities in the two waveguides. Based on this discrepancy, Sharoglazova et al. questioned the physical interpretation of the Bohmian velocity.

Here we identify two closely related questions. First, which of these two velocity definitions provides a physically meaningful characterization of the particle’s local motion in the evanescent region? Second, if the Bohmian velocity vanishes in an evanescent state, how can one consistently account for the particle’s residence within the

barrier? Addressing these questions requires going beyond conventional steady-state analyses [18, 19], which by construction suppress transient dynamics. We consider a wave function $\psi(x, t)$ with its intensity having a finite rise time, plateau, and fall time, as shown in Fig. 1(d), and compute the full dynamical tunnelling process with a time-dependent Schrödinger equation. This allows us to extract the time-dependent velocity $\mathbf{v}(x, t)$ and probability density $\rho(x, t)$ inside the barrier. As illustrated in Fig. 1(e), the probability density within the barrier is nonzero, while the velocity remains to be determined.

RESULTS

The pulse under consideration travels along the x -axis and strikes a potential barrier perpendicularly. Its full width at half maximum is 1.14 ns, with a flat-top region lasting 0.86 ns. We simulate the entire 2.18 ns duration from incidence to reflection. From initial moment $t = 0$ to $t = 0.86$ ns, the pulse’s leading edge interacts with the barrier; At $t = 0.86$ ns, the right edge of the pulse plateau reaches the left boundary of the potential barrier. By $t = 1.72$ ns, the left edge of the plateau reaches the left boundary, concluding the interaction between the entire plateau region and the barrier. The falling and rising edges of the pulse exhibit symmetry about the pulse centre. The potential V is zero in the region where $x < 0$, and in the region where $x \geq 0$, it is $V_0 = 0.538$ meV. By controlling the energy E of the particle, we simulate the tunnelling process in three distinct energy regions, namely $\Delta = E - V_0 > 0$, $\Delta = 0$, and $\Delta < 0$. Since the particle possesses no potential energy at the initial moment, its energy is determined by the kinetic energy, $E = mv^2/2$ with $m = 6.95 \times 10^{-36}$ kg.

We first simulate the one-dimensional tunnelling process by solving the time-dependent Schrödinger equation to obtain the wave function $\psi(x, t)$, then determine the Bohmian velocity according to Eq. (1) (see the Methods for further details). The pseudocolour images in Fig. 2 illustrate the probability distribution within the potential barrier at $t = 1.09$ ns (approximately the moment when the midpoint of the pulse plateau reaches the left boundary of the barrier), with each plot normalised to its own maximum value. For $\Delta = 0.1$ meV, the wave packet can maintain its forward propagation mode even within the barrier, as its energy exceeds that of the barrier. As can be seen from Fig. 2(a), the wave function penetrates deep into the potential wall. We select three points near the left boundary of the potential, marked respectively by a red circle, a green triangle, and a blue square. The instantaneous velocities at these three spatial positions are depicted by the curves bearing the corresponding markers. The speed decreased from approximately 5000 km/s to around 2000 km/s. When $\Delta = 0$, the wave function

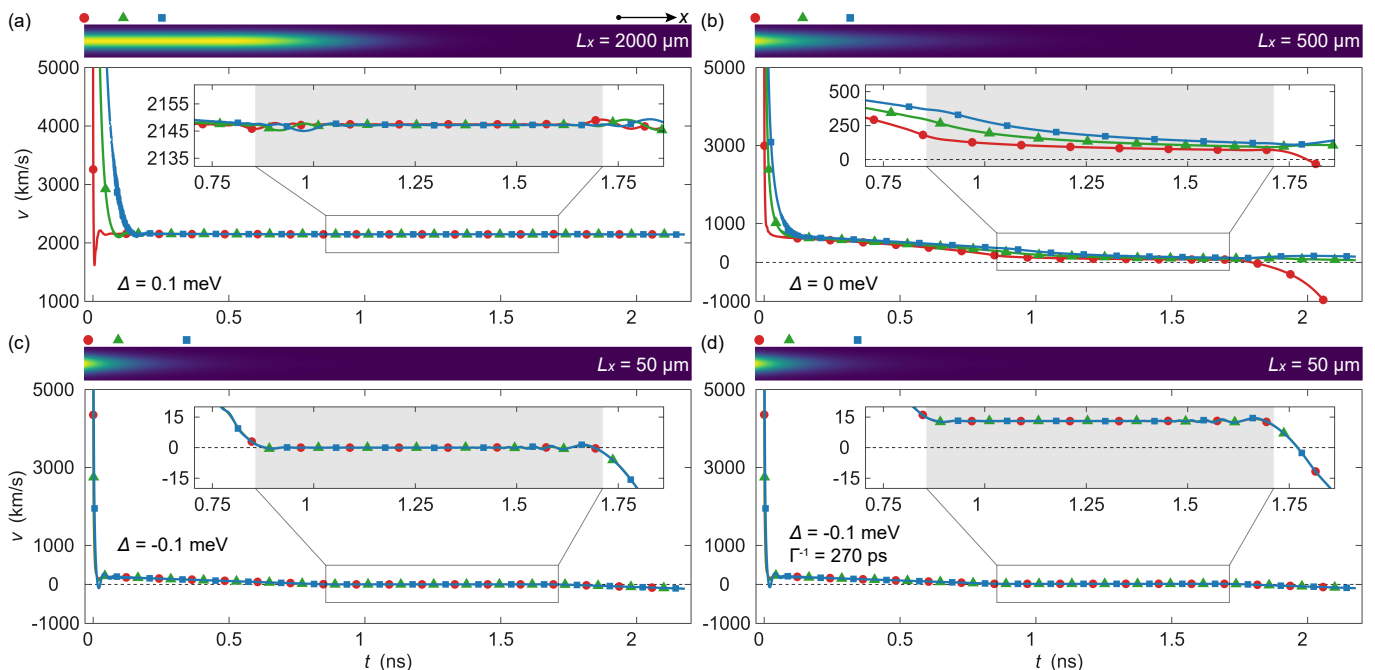


FIG. 2. **Instantaneous Bohmian velocity of a one-dimensional wave packet encountering a potential barrier.** The wave packet propagates along the x -axis, and the pseudocolor plot shows the spatial distribution of the probability density at $t = 1.09$ ns. Each plot is normalised to its maximum value. The left edge of each pseudocolor panel corresponds to the entrance of the barrier, while the right edge corresponds to $x = L_x$. The barrier height is fixed at $V_0 = 0.538$ meV. Panels (a), (b), and (c) correspond to energy detunings $\Delta = E - V_0 = 0.1$ meV, 0 meV, and -0.1 meV, respectively. In each panel, three markers—red circles, green triangles, and blue squares—denote three spatial locations inside the barrier, and the time evolution of the Bohmian velocity at these positions is plotted using curves with the corresponding markers. In (a), the three positions have depths of 0.425 μm , 128.79 μm , and 256.30 μm . In (b), the depths are 0.39 μm , 39.42 μm , and 78.45 μm . In (c) and (d), the depths are 0.35 μm , 2.82 μm , and 8.45 μm . The gray shaded region corresponds to the time period during which the pulse flat-top interacts with the barrier, from 0.86 ns to 1.71 ns. Panel (d) uses the same detuning as (c), $\Delta = -0.1$ meV, but incorporates a finite particle lifetime of $\Gamma^{-1} = 270$ ps, corresponding to a dissipation rate of $\Gamma \approx 3.7$ GHz.

within the potential barrier is not a travelling wave; instead, it decays with distance within the barrier, as illustrated in Fig. 2(b) (note that the probability density plot region is $L_x = 500$ μm , not the 2000 μm used in Fig. 2(a)). The velocities at the three positions within the barrier also decrease over time, but drop below 250 km/s. The zoomed-in diagram illustrates the time interval (grey shaded area) during which the pulse’s flat-top portion encounters the barrier. During the pulse plateau phase, the change in velocity over time is small, particularly at the red dot closest to the barrier boundary.

This phenomenon is more pronounced when $\Delta < 0$. Figure 2(c) illustrates the variation of velocity with time for $\Delta = -0.1$ meV. At this point, the wave function exhibits stronger decay within the potential barrier, with the three sites selected closer to the boundary. The velocities at these three points remain zero throughout the duration of the pulse plateau (grey shaded area), but are nonzero when the pulse plateau has not yet arrived or has already departed from the barrier. The speed undergoes a “positive-zero-negative” transition over time, indicating that within the decay mode region, the entire tunnelling process can be divided into three distinct

phases: “entry-stationary-exit”. To further investigate the origin of the steady state, we introduce dissipation into the wave function within the potential barrier by setting a finite particle lifetime of 270 ps. The results are shown in Fig. 2(d), where the particle velocity remains stable within the pulse plateau region, yet is not zero but rather 13 km/s. For $\Delta = 0$, the velocity distribution inside the barrier approaches its steady state more slowly than in the cases $\Delta = \pm 0.1$ meV, and no clear transition point is observed at the onset of the pulse flat-top ($t = 0.86$ ns). All three velocity curves fail to converge to their steady-state values at the end of the flat-top region, indicating that $\Delta = 0$ corresponds to a distinct dynamical process.

When the amplitude of the incident wave function remains unchanged, a zero velocity can emerge within the potential barrier. This is a counterintuitive phenomenon. We further examined scenarios where, following tunnelling, the wave packet can be partially transported to another auxiliary system. This can be simplified to tunnelling within a “two-dimensional” system comprising two waveguides. We retain the previous wave packet parameters. The wave packet initially resides in

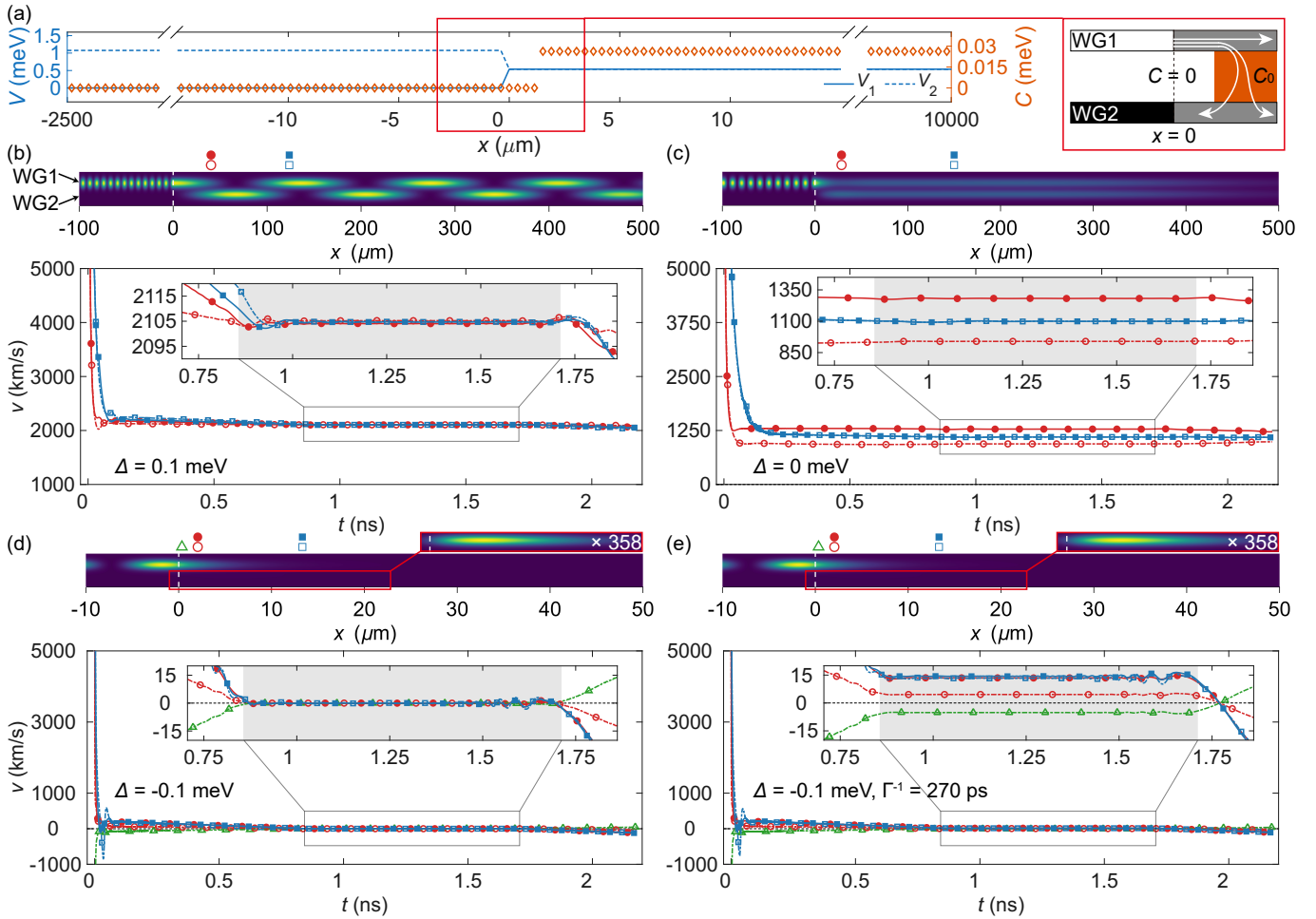


FIG. 3. Evolution of a one-dimensional wave packet in two coupled waveguides after encountering a potential barrier. (a) Potential profiles of waveguide 1 (WG1, solid blue) and waveguide 2 (WG2, dashed blue), together with the inter-waveguide coupling strength C (orange diamonds). WG1 has $V_1 = 0$ for $x < 0$ and $V_1 = V_0 = 0.538$ meV for $x \geq 0$. WG2 has $V_2 = 2V_0$ for $x < 0$ and $V_2 = V_0$ for $x \geq 0$. The coupling is switched on at $x = 1.25 \mu\text{m}$, $1.14 \mu\text{m}$ and $1.02 \mu\text{m}$ for $\Delta = 0.1$ meV, 0 meV and -0.1 meV respectively, with a strength of $26.22 \mu\text{eV}$, as illustrated on the right. (b-e) The pseudocolor plot shows the spatial distribution of the probability density in the two waveguides at $t = 1.09$ ns. Each plot is normalised to its maximum value. The energy detunings are $\Delta = 0.1$ meV for (b), $\Delta = 0$ for (c), and $\Delta = -0.1$ meV for (d) and (e). The gray shaded region corresponds to the time period during which the pulse flat-top interacts with the barrier, from 0.86 ns to 1.71 ns. For each panel, the time-dependent Bohmian velocities are plotted for two or three selected positions on each waveguide; red circles and blue squares mark the spatial locations, while filled and open versions of each marker denote the sampling points on waveguide 1 and waveguide 2, respectively. In (b), the positions are $x = 40.37 \mu\text{m}$ and $123.62 \mu\text{m}$. In (c), the positions are $x = 28.55 \mu\text{m}$ and $149.99 \mu\text{m}$. In (d) and (e), the positions are $x = 5.46 \mu\text{m}$ and $13.32 \mu\text{m}$. For WG2, an additional velocity trace is shown for the position $x = 2.05 \mu\text{m}$. A finite particle lifetime of $\Gamma^{-1} = 270$ ps is applied in (d).

waveguide 1 (WG1, main waveguide) extending along the x -axis, where the potential energy is zero. The potential barrier of WG1 lies in the region $x \geq 0$, with a height of V_0 . After traversing approximately $1 \mu\text{m}$ of the barrier, the particle begins to couple to waveguide 2 (WG2, auxiliary waveguide) with a weak coupling efficiency C_0 , as indicated in Fig. 3(a). To prevent particles in WG2 from migrating excessively into regions uncoupled from WG1, we introduce a high barrier of $2V_0$ for WG2 in the region where $x < 0$. Three scenarios are simulated: $\Delta = E - V_0 + \hbar C_0 > 0$, $\Delta = 0$, and $\Delta < 0$.

For $\Delta = 0.1$ meV, the pseudocolor image in Fig. 3(b) displays the spatial distribution of the normalised probability density, corresponding to the time at which the pulse's flat-top midpoint propagates to the barrier boundary. Under the given conditions, the wave packet oscillates continuously along the x -axis between the two waveguides. We select two positions where the probability density of the auxiliary waveguide reached half its maximum value, indicated by the red circle and blue square. Solid and hollow markers denote sampling points on the main and auxiliary waveguides respectively. The

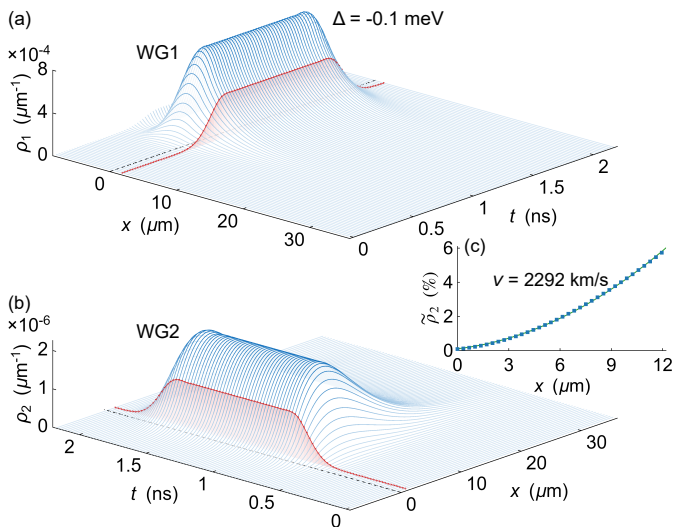


FIG. 4. **Evolution of probability density distributions in the main and auxiliary waveguides for $\Delta = -0.1$ meV.** (a) Time evolution of the probability density ρ_1 in the main waveguide (WG1). (b) Time evolution of the probability density ρ_2 in the auxiliary waveguide (WG2). The red plane represents the cross-section at $x = 1.37 \mu\text{m}$, and the red curve shows the variation of the probability density at this position over time. Between $t = 0.86$ ns and $t = 1.71$ ns, the flat-top portion of the incident pulse interacts with the barrier, during which the red curve becomes parallel to the time axis, indicating no change in probability density. (c) At $t = 1.09$ ns, the proportion of probability density in the auxiliary waveguide, defined as $\tilde{\rho}_2 = \rho_2 / (\rho_1 + \rho_2)$, is plotted as a function of spatial distance. The data is fitted using $\tilde{\rho}_2 = (C_0(x - x_0)/v)^2$, yielding a “steady-state velocity” of particles in the auxiliary waveguide $v = 2292$ km/s (with fitting parameter $x_0 = -1.91 \mu\text{m}$ and the goodness of fit $R^2 = 0.9997$). This result contrasts with the zero velocity observed in the flat-top region of Fig. 3(d).

velocity evolution curves for these four positions are labelled with corresponding markers. It can be observed that during the pulse plateau phase, these velocities stabilised at approximately 2105 km/s, significantly exceeding zero. Figure 3(c) depicts the case where $\Delta = 0$, at which point the velocities at the four positions within the barrier are around 1000 km/s during the pulse plateau phase. A peculiar phenomenon occurs at $\Delta = -0.1$ meV, as illustrated in Fig. 3(d). The velocities of all five points within the potential barrier (two in the main waveguide and three in the auxiliary waveguide) vanish entirely during the pulse plateau phase. Compared to the one-dimensional scenario presented in Fig. 2(c), an additional case arises here: the velocity at the green hollow triangle first becomes negative, then vanishes, and finally turns positive. This occurs because this position lies to the left of the coupling region (see Fig. 3(a)) between the two waveguides. During the pulse’s rising edge, particles flow through this position from right to left within WG2 (velocity along the $-x$ direction). During the pulse’s plateau

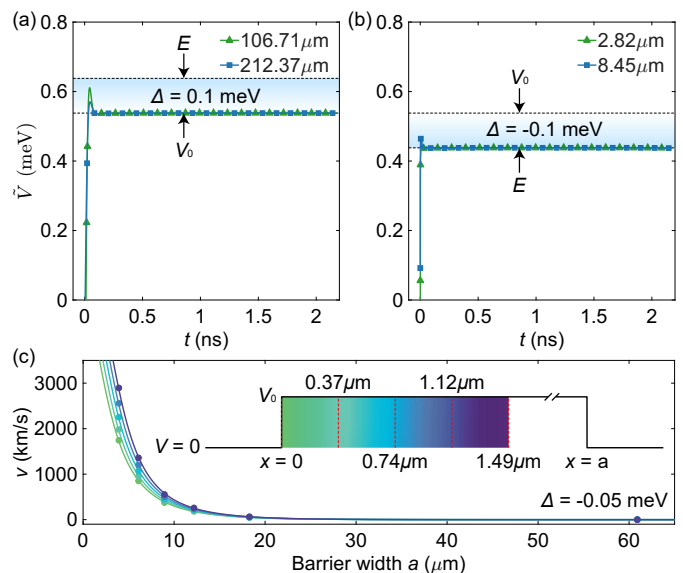


FIG. 5. **Time evolution of the effective potential.** (a) For $\Delta = 0.1$ meV, the curves with green triangles and blue squares correspond to the time evolution of the effective potential $\tilde{V} = Q + V_0$ at positions $x = 106.71 \mu\text{m}$ and $x = 212.37 \mu\text{m}$, respectively. (b) For $\Delta = -0.1$ meV, the curves with green triangles and blue squares correspond to the time evolution of the effective potential \tilde{V} at positions $x = 2.82 \mu\text{m}$ and $x = 8.45 \mu\text{m}$, respectively. In both panels, the energy E and the barrier height V_0 are indicated by arrows. The blue shaded regions, with the gradient direction reversed, directly reflects the relative height of E with respect to V_0 . (c) Dependence of the steady-state velocity on the barrier width for $\Delta = -0.05$ meV. The five curves represent the function $v(x) = v_0 / [1 + (V_0/|\Delta|) \sinh^2(\kappa(x - a))]$ evaluated at different spatial positions x . Colors indicate distinct locations along the x -axis, as shown by the color bar embedded within a potential barrier of width a . Numerical results are denoted by filled circles; see Methods for derivation details.

phase, particles remain stationary. On the falling edge, particles flow through this position from left to right (velocity along the $+x$ direction), thereby exiting WG2. We further examined the case with dissipation, as shown in Fig. 3(e), obtaining velocities of approximately 10 km/s, which is similar to the one-dimensional case in Fig. 2(d).

Zero velocity within the barrier should correspond to a stable probability density distribution. To clarify this point, we present the probability densities for the main and auxiliary waveguides, as shown in Fig. 4. It can be seen that a portion of the wave function enters the potential barrier, only to be reflected back together with the portion that did not enter the barrier. The red shaded region denotes the plane at $x = 1.37 \mu\text{m}$, approximately corresponding to the location of the red circle in Fig. 2(c). Its intersection with the probability density profile is shown by the red curve. This curve exhibits distinct rising and falling edges, remaining constant during the pulse plateau phase (from $t = 0.86$ ns to $t = 1.72$ ns), aligning

with the outcome of particles being “frozen” within the potential barrier. In a recent study [23], a sort of velocity was defined by a parabolic fit of the relative probability density $\tilde{\rho}_2 = \rho_2 / (\rho_1 + \rho_2)$ in the steady-state region. Here, we fit the data shown in Fig. 4(c) with a parabolic function $\tilde{\rho}_2 = (C_0(x - x_0)/v)^2$ at $t = 1.09$ ns (within the steady-state region), yielding $v = 2292$ km/s, which corresponds with the results in Ref. [23]. This “steady-state velocity,” determined solely by the probability densities, hardly reflects the true velocity of particles within the barrier, particularly in the evanescent region. Conversely, the Bohmian speed experimentally measured in Ref. [23] approaches zero, consistent with our observation that particle velocity vanishes in steady-state conditions.

To further elucidate why particles can enter the potential barrier at high velocity yet gradually become stationary, we examine the relationship between the effective potential $\tilde{V} = Q + V_0$ and the particle’s energy E . In Bohmian mechanics, $Q = -\hbar^2 \nabla^2 R / (2mR)$ is defined as the quantum potential. Figure 5(a) illustrates the evolution of the effective potential over time at two distinct sites when $\Delta = 0.1$ meV. It is evident that when the wave packet initially enters the barrier, the effective potential is significantly below E , resulting in high particle velocities. As the wave packet progresses into the barrier, the effective potential rapidly rises to V_0 , indicating that the quantum potential gradually approaches zero. At this point, the classical potential dominates; however, since $E > V_0$, the particle always maintains an appropriate velocity of around 2145 km/s, as depicted in Fig. 2(a). For $\Delta = -0.1$ meV, the effective potential also undergoes a rapid ascent, as shown in Fig. 5(b). It is during this process that, owing to the profoundly negative quantum potential, particles can traverse the barrier boundary. However, when the effective potential rises to a level comparable to E , the particle’s kinetic energy dissipates, its velocity becomes zero, and it ceases to move.

By contrast, we remark that when the potential barrier width is finite, the particles exhibit different steady-state dynamics. By taking the spatial gradient of the phase of the steady-state solution, we obtain the steady-state velocity

$$v_{\Delta < 0}(x) = \frac{v_0}{1 + \frac{V_0}{|\Delta|} \sinh^2[\kappa(x - a)]} \quad (2)$$

for $\Delta < 0$, where a is the barrier width. See Methods for steady-state velocities with $\Delta > 0$ and $\Delta = 0$. In Fig. 5(c), we present the dependence of the steady-state velocity on the barrier width for $\Delta = -0.05$ meV. When the barrier width is small, the velocity inside the barrier can be large, and positions farther from the left boundary of the barrier correspond to higher velocities. As the barrier width increases toward infinity, the velocity inside the barrier approaches zero, indicating that the particle becomes effectively frozen within the barrier. This result

is consistent with Fig. 2(c), where a semi-infinite barrier is considered.

DISCUSSION

Our results reveal that during the rising edge of the incident wave packet, the particle velocity inside the barrier is nonzero, indicating rapid entry into the barrier. During the plateau stage, the velocity inside the barrier vanishes, corresponding to zero probability current density, $j = \rho v = 0$, and recovering the familiar steady-state solution in the evanescent state. In this situation, the probability current density j vanishes. However, this does not imply that the dwell time $\tau_{\text{dwell}} = N/j$ diverges, where N denotes the number of particles frozen inside the barrier. A pulse with a perfectly flat top but without rising and falling edges is not physical; realistic wave packets necessarily possess finite temporal gradients and finite dissipation, which regularize the dwell time. If one attempts to define a particle velocity from the probability density rather than from the probability current, the resulting quantity can be spurious, leading to an apparent velocity, such as 2292 km/s, as illustrated in Fig. 4(c). During the falling edge, the velocity reverses sign, indicating that the particle exits the barrier. Correspondingly, the probability distribution ρ inside the barrier is built up during the rising edge, remains constant during the plateau, and gradually vanishes during the falling edge. These results resolve the two questions raised in the Introduction and provide a coherent physical picture of tunnelling dynamics. Notably, the transient causal flow underlying tunnelling, uncovered here, lies beyond the reach of conventional steady-state analyses and offers new insights into the time-resolved observation of tunnelling phenomena.

Experimentally, several rapidly developing directions make it realistic to expect decisive tests. Optical-lattice and cold-atom platforms permit highly controlled, programmable barriers and have already been used to directly access tunnelling delay in lattice potentials [25, 26], offering an ideal testbed for comparing local-velocity-based predictions to wave-packet and phase-based measures. On the ultrafast front, attosecond metrology and attoclock protocols provide access to sub-femtosecond ionization and tunnelling times [27, 28], enabling time-domain comparisons between local-flow predictions and strong-field timing observables. Recent theoretical and experimental work showing negative excitation times or negative group delays for photon-atom systems highlights the subtle role of dispersion, energy storage and interference; these results indicate that group delay or excitation-time measurements can be negative without violating causality, and motivate hybrid probe schemes that can directly relate local probability flow to measured delays [11, 29].

In this work, we focus on the instantaneous velocity

inside a potential barrier, from which one can qualitatively infer the tunnelling dwell time within a continuity-equation-based framework. Such a dwell time can differ systematically from other, widely used tunnelling-time definitions, for example group delay. Group delay typically reflects wave-packet peak propagation, while a continuity-equation dwell time reflects local probability flow through the barrier. This distinction aligns with critical analyses of purported “superluminal” tunnelling and shows that apparent contradictions often reduce to mismatches between which physical observable is being measured. We argue that focusing on the instantaneous velocity distribution inside the barrier, combined with programmable quantum-simulation platforms, advanced waveguide and photonic-chip micro- and nano-fabrication technologies [30], weak measurements [31–34] and high-resolution time-domain detection techniques [27, 28, 35], offers a promising route toward clarifying the long-standing debate on tunnelling time. Rather than seeking a single “correct” definition, this perspective emphasizes identifying the specific physical quantity and operational regime probed according to each definition.

* These authors contributed equally to this work.

† These authors contributed equally to this work; doujianpeng@sjtu.edu.cn

‡ htang2015@sjtu.edu.cn

§ xianmin.jin@sjtu.edu.cn

1. Dewdney, C. & Hiley, B. J. A Quantum Potential Description of One-Dimensional Time-Dependent Scattering From Square Barriers and Square Wells. *Found. Phys.* **12**, 27-48 (1982).
2. Jayannavar, A. M. A note on traversal time for tunneling. *Pramana* **29**, 341-344 (1987).
3. Winful, H. G. Tunneling time, the Hartman effect, and superluminality: A proposed resolution of an old paradox. *Phys. Rep.* **436**, 1-69 (2006).
4. Landauer, R. & Martin, Th. Barrier interaction time in tunneling. *Rev. Mod. Phys.* **66**, 217-228 (1994).
5. Ranfagni, A., Mugnai, D., Fabeni, P. & Pazzi, G. P. Delay-time measurements in narrowed waveguides as a test of tunneling. *Appl. Phys. Lett.* **58**, 774-776 (1991).
6. Enders, A. & Nimtz, G. On superluminal barrier traversal. *J. Phys. I* **2**, 1693-1698 (1992).
7. Steinberg, A. M., Kwiat, P. G. & Chiao, R. Y. Measurement of the single-photon tunneling time. *Phys. Rev. Lett.* **71**, 708-711 (1993).
8. Spielmann, Ch., Szipöcs, R., Stingl, A. & Krausz, F. Tunneling of Optical Pulses through Photonic Band Gaps. *Phys. Rev. Lett.* **73**, 2308-2311 (1994).
9. Katsnelson, M. I., Novoselov, K. S. & Geim, A. K. Chiral tunnelling and the Klein paradox in graphene. *Nature Phys.* **2**, 620-625 (2006).
10. Ramos, R., Spierings, D., Racicot, I. & Steinberg, A. M. Measurement of the time spent by a tunnelling atom within the barrier region. *Nature* **583**, 529-532 (2020).
11. Angulo, D. et al. Experimental evidence that a photon can spend a negative amount of time in an atom cloud. Preprint at arXiv <https://doi.org/10.48550/arXiv.2409.03680> (2024).
12. Bohm, D. A Suggested Interpretation of the Quantum Theory in Terms of “Hidden” Variables. I. *Phys. Rev.* **85**, 166-179 (1952).
13. Dürr, D., Goldstein, S., Zanghi, N. Quantum equilibrium and the origin of absolute uncertainty. *J. Stat. Phys.* **67**, 843-907 (1992).
14. Sanz, A. S. & Miret-Artés, S. Quantum phase analysis with quantum trajectories: A step towards the creation of a Bohmian thinking. *Am. J. Phys.* **80**, 525–533 (2012).
15. Nikolic, H. Overcoming a challenge for Bohmian mechanics. Preprint at <https://doi.org/10.48550/arXiv.2507.08049> (2025).
16. Sienicki, M. & Sienicki, K. Critical Reflections on Overcoming a Challenge for Bohmian Mechanics by H. Nikolic and the Experimental Findings of Sharoglazova et al. Preprint at <https://doi.org/10.48550/arXiv.2507.10989> (2025).
17. Dickau, M. Apparent energy-speed relationship poses no challenge to Bohmian mechanics. Preprint at <https://doi.org/10.48550/arXiv.2507.18826> (2025).
18. Wang, Y.-F., Wang, X.-Y., Wang, H. & Lu, C.-Y. Tunneling photons pose no challenge to Bohmian mechanics. Preprint at <https://doi.org/10.48550/arXiv.2507.20101> (2025).
19. Drezet, A., Lazarovici, D. & Nabet, B. M. Comment on “Energy-speed relationship of quantum particles challenges Bohmian mechanics”. Preprint at <https://doi.org/10.48550/arXiv.2508.04756> (2025).
20. Daem, F., Durt, T. & Matzkin, A. Trajectories in coupled waveguides: an application to a recent experiment and Hiley’s lessons on the falsification of the Bohmian model. Preprint at <https://doi.org/10.48550/arXiv.2510.21504> (2025).
21. Waegell, M. Is Bohmian mechanics missing some motion? Why a recent experiment is inconclusive. Preprint at <https://doi.org/10.48550/arXiv.2511.17215> (2025).
22. Drezet, A. & Nabet, B. M. Formal equivalence between Maxwell equations and the de Broglie-Bohm theory for two-dimensional optical microcavities. Preprint at <https://doi.org/10.48550/arXiv.2512.01671> (2025).
23. Sharoglazova, V., Puplauskis, M., Mattschas, C., Toebes, C. & Klaers, J. Energy-speed relationship of quantum particles challenges Bohmian mechanics. *Nature* **643**, 67-72 (2025).
24. Klaers, J., Sharoglazova, V. & Puplauskis, M. Reaffirming a Challenge to Bohmian Mechanics. Preprint at <https://doi.org/10.48550/arXiv.2509.06584> (2025).
25. Fortun, A. et al. Direct Tunneling Delay Time Measurement in an Optical Lattice. *Phys. Rev. Lett.* **117**, 010401 (2016).
26. Yang, Y. X., Bai, S. Y. & An, J. H. Long-range quantum tunneling via matter waves. *Commun. Phys.* **8**, 5 (2025).
27. Sainadh, U. S. et al. Attosecond angular streaking and tunnelling time in atomic hydrogen. *Nature* **568**, 75-77 (2019).
28. Orunesajo, E. et al. Phase-Resolved Attoclock. *Phys. Rev. Lett.* **134**, 203201 (2025).
29. Thompson, K. et al. How much time does a photon spend as an atomic excitation before being transmitted through

- a cloud of atoms? *APL Quantum* **2**, 036108 (2025).
30. Zhong, L., Wang, Y., Han, X., Hu, J. & Qiu, J. Laser direct lithography of large-area three-dimensional integrated photonics: Technological challenges and advances. *Chip* **4**, 100157 (2025).
 31. Kocsis, S. et al. Observing the Average Trajectories of Single Photons in a Two-Slit Interferometer. *Science* **332**, 1170 (2011).
 32. Zimmermann, T., Mishra, S., Doran, B. R., Gordon, Daniel F. & Landsman, A. S. Tunneling Time and Weak Measurement in Strong Field Ionization. *Phys. Rev. Lett.* **116**, 233603 (2016).
 33. Foo, J., Asmodelle, E., Lund, A. P. & Ralph, T. C. Relativistic Bohmian trajectories of photons via weak measurements. *Nat. Commun.* **13**, 4002 (2022).
 34. Dou, J.-P., Lu, F., Tang, H. & Jin, X.-M. Test of Nonlocal Energy Alteration between Two Quantum Memories. *Phys. Rev. Lett.* **134**, 093601 (2025).
 35. Hogenbirk, E. et al. Intensified optical camera with Timepix4 readout. Preprint at <https://doi.org/10.48550/arXiv.2509.14649> (2025).

METHODS

Models and numerical methods

For the one-dimensional case, the Schrödinger equation with full time dependence is expressed as

$$i\hbar \frac{\partial}{\partial t} \psi(x, t) = \left[-\frac{\hbar^2}{2m} \frac{\partial^2}{\partial x^2} + V(x) \right] \psi(x, t). \quad (3)$$

To solve the wave function, we employ the Split-Step Fourier Method (SSFM), namely calculating the evolution operator using

$$\hat{U} \approx e^{-\frac{i}{\hbar} \hat{T} \frac{\Delta t}{2}} e^{-\frac{i}{\hbar} \hat{V} \Delta t} e^{-\frac{i}{\hbar} \hat{T} \frac{\Delta t}{2}} + \mathcal{O}(\Delta t^3), \quad (4)$$

where Δt is the time step and $\hat{T} = -\frac{\hbar^2}{2m} \frac{\partial^2}{\partial x^2}$ is an operator that contains only kinetic energy. The particle mass is 6.95×10^{-36} kg. The potential $V(x)$ is equal to 0.538 meV in the region where $x \geq 0$, and $V(x) = 0$ in all other regions. Throughout the numerical calculations for the one-dimensional waveguide, the initial pulse is assigned a fixed full width at half maximum (FWHM) of 1.14 ns, and the barrier height V_0 is fixed at 0.538 meV. The spatial ranges of the simulation boxes are respectively from -13.93 mm to 13.93 mm for $\Delta = 0.1$ meV, from -12.79 mm to 12.79 mm for $\Delta = 0$, and from -11.54 mm to 11.54 mm for $\Delta = -0.1$ meV. The evolution of the wave function is simulated over a time span from 0 to 2.18 ns, a duration sufficient for the majority of the reflected wave to depart from the left boundary of the potential barrier. At the initial moment, the centres of the wave packets are located at -6.96 mm for $\Delta = 0.1$ meV, -6.40 mm for $\Delta = 0$, and -5.77 mm for $\Delta = -0.1$ meV. The full widths at half maximum of the packet are in space are 6.19 mm for $\Delta = 0.1$ meV, 5.68 mm for $\Delta = 0$,

and 5.13 mm for $\Delta = -0.1$ meV. The spatial widths of the wave packet's flat top are 4.64 mm for $\Delta = 0.1$ meV, 4.26 mm for $\Delta = 0$, and -3.85 mm for $\Delta = -0.1$ meV.

For the case of two waveguides, the Schrödinger equation is written as

$$i\hbar \frac{\partial}{\partial t} \psi_1(x, t) = \left[-\frac{\hbar^2}{2m} \frac{\partial^2}{\partial x^2} + V(x) \right] \psi_1(x, t) + \hbar C(x) [\psi_2(x, t) - \psi_1(x, t)], \quad (5)$$

$$i\hbar \frac{\partial}{\partial t} \psi_2(x, t) = \left[-\frac{\hbar^2}{2m} \frac{\partial^2}{\partial x^2} + V(x) \right] \psi_2(x, t) + \hbar C(x) [\psi_1(x, t) - \psi_2(x, t)], \quad (6)$$

where $C(x)$ refers to the coupling strength. The regions where the coupling energy $\hbar C(x)$ assumes the value $26.22 \mu\text{eV}$ are $x \geq 1.25 \mu\text{m}$, $x \geq 1.14 \mu\text{m}$, and $x \geq 1.02 \mu\text{m}$, respectively, for $\Delta = 0.1$ meV, $\Delta = 0$ and $\Delta = -0.1$ meV. In other regions, the coupling vanishes. The other parameters are similar to those in the one-dimensional case.

Particle velocity within a square barrier

Consider a particle with energy E incident along the positive x -axis into a square potential barrier

$$V(x) = \begin{cases} V_0, & \text{if } 0 < x < a; \\ 0, & \text{if } x < 0, x > a. \end{cases} \quad (7)$$

1) When $E < V_0$, the time-independent Schrödinger equation for the region inside the potential barrier reads

$$\left[-\frac{\hbar^2}{2m} \frac{d^2}{dx^2} + V_0 \right] \psi(x) = E\psi(x), \quad (8)$$

for $0 < x < a$. The general solution of the energy eigenfunction in this region has the form

$$\psi(x) = Ae^{\kappa x} + Be^{-\kappa x}, \quad (9)$$

with $\kappa = \sqrt{2m(V_0 - E)}/\hbar^2$ a positive constant. Note that in Eq. (9), there exists not only an exponentially decaying term but also an exponentially growing term. This differs from the form of the steady-state solution for the semi-infinite potential barrier considered in the main text. In the latter case, since a is positive infinity, the coefficient of the growing component (i.e. A) must be exactly zero to prevent the wave function from diverging. Based on the continuity conditions for the wave function and its derivative at $x = a$, we have

$$A = \frac{T}{2} \left(1 + \frac{ik}{\kappa} \right) e^{ika - \kappa a}, \quad (10)$$

$$B = \frac{T}{2} \left(1 - \frac{ik}{\kappa} \right) e^{ika + \kappa a}, \quad (11)$$

where $k = \sqrt{2mE/\hbar^2}$ is the modulus of the incident wave's wave vector, and T is the coefficient of the wave function Te^{ikx} in the region $x > a$, with only transmitted waves present. Here emerges the indication that particles in the potential barrier exhibit nonzero velocities in steady state: coefficients A and B are complex numbers, and their respective proportions (real-valued $e^{\kappa x}$ and $e^{-\kappa x}$) vary with x , causing the phase angle S of the wave function $\psi = |\psi|e^{iS}$ to change with x . We express the tangent of S as the ratio of the wave function's real and imaginary parts, yielding $\tan[S] = \text{Im}[\psi]/\text{Re}[\psi]$ to be expressed as

$$\frac{e^{\kappa(x-a)} \left(\sin ka + \frac{k}{\kappa} \cos ka \right) + e^{-\kappa(x-a)} \left(\sin ka - \frac{k}{\kappa} \cos ka \right)}{e^{\kappa(x-a)} \left(\cos ka - \frac{k}{\kappa} \sin ka \right) + e^{-\kappa(x-a)} \left(\cos ka + \frac{k}{\kappa} \sin ka \right)} \quad (12)$$

Substituting $F = \tan[S]$ into the spatial derivative of S

$$v(x) = \frac{\hbar}{m} \frac{\partial S}{\partial x} = \frac{\hbar}{m} \frac{1}{1+F^2} \frac{\partial F}{\partial x}, \quad (13)$$

we obtain the particle's velocity within the potential barrier

$$v_{\Delta < 0}(x) = \frac{v_0}{1 + \frac{V_0}{|\Delta|} \sinh^2[\kappa(x-a)]}, \quad (14)$$

where $v_0 = \hbar k/m$ is the velocity of the incident particle. When the barrier width a is finite, the velocity v inside the barrier is distinctly nonzero. In contrast, when a becomes sufficiently large, the velocity within the barrier approaches zero over an extended region, particularly near the left side of the barrier. If the right boundary of the potential barrier is removed (i.e. a step potential barrier), the coefficient of the growth term in Eq. (9) must be discarded, resulting in a constant S within the barrier and the particle velocity being strictly zero.

2) When $E = V_0$, the wave function inside the potential barrier takes the form

$$\psi(x) = A + Bx. \quad (15)$$

Through similar derivation, we obtain the velocity of particles within the potential barrier

$$v_{\Delta=0}(x) = \frac{v_0}{1 + k^2(x-a)^2}. \quad (16)$$

Similar to the case where $E < V_0$, for the step potential, the linear term in Eq. (15) cancels out, necessitating that particles within the potential barrier remain strictly stationary.

3) When $E > V_0$, the general solution for the wave function inside the potential barrier reads

$$\psi(x) = Ae^{ik'x} + Be^{-ik'x}, \quad (17)$$

where $k' = \sqrt{2m(E - V_0)/\hbar^2}$. The corresponding velocity is calculated as

$$v_{\Delta > 0}(x) = \frac{v_0}{1 + \frac{V_0}{|\Delta|} \sin^2[k'(x-a)]}. \quad (18)$$

For energies above the barrier, the stationary solution inside a finite-width barrier necessarily contains both forward- and backward-propagating components, which leads to spatial oscillations in the velocity profile. In contrast, if the particle is allowed to impinge only from the left boundary of the barrier, for example, in the case of a semi-infinite barrier (i.e. a step potential), then the backward-propagating component can be removed. This restriction results in a much simpler velocity distribution

$$v_{\Delta > 0}(x) = \sqrt{\frac{2(E - V_0)}{m}}. \quad (19)$$

Substituting the simulation parameters yields $v_{\Delta > 0}(x) = 2147$ km/s, which is consistent with the results shown in Fig. 2(a). In numerical calculations, a semi-infinite barrier can be effectively emulated by introducing an absorbing layer inside the barrier, placed sufficiently far from the left boundary. This absorbing region completely suppresses the left-propagating component of the wave function, thereby eliminating the reflections and reproducing the behavior of a semi-infinite barrier.